Platinum-Paper Micromotors: An Urchin-like Nanohybrid Catalyst for Green Monopropellant Bubble-Thrusters

Jonathan C. Claussen,[*,†] Michael A. Daniele,[‡] Jason Geder,[§] Marius Pruessner,[‡] Antti J. Mäkinen,[∥] Brian J. Melde,[‡] Mark Twigg,[⊥] Jasenka M. Verbarg,[‡] and Igor L. Medintz[‡]

[†]Department of Mechanical Engineering, Iowa State University, 2104 Black Engineering, Ames, Iowa 50011, United States
[‡]Center for Bio/Molecular Science & Engineering, Code 6900, [§]Laboratories for Computational Physics and Fluid Dynamics, Code 6041, [∥]Optical Sciences Division, Code 5600, [⊥]Electronics Science and Technology Division, Code 6876, U.S. Naval Research Laboratory, 4555 Overlook Avenue SW, Washington, DC 20375, United States

Ⓢ *Supporting Information*

ABSTRACT: Platinum nanourchins supported on micro-fibrilated cellulose films (MFC) were fabricated and evaluated as hydrogen peroxide catalysts for small-scale, autonomous underwater vehicle (AUV) propulsion systems. The catalytic substrate was synthesized through the reduction of chloroplatinic acid to create a thick film of Pt coral-like microstructures coated with Pt urchin-like nanowires that are arrayed in three dimensions on a two-dimensional MFC film. This organic/inorganic nanohybrid displays high catalytic ability (reduced activation energy of 50−63% over conventional materials and 13−19% for similar Pt nanoparticle-based structures) during hydrogen peroxide (H_2O_2) decomposition

as well as sufficient propulsive thrust (>0.5 N) from reagent grade H_2O_2 (30% w/w) fuel within a small underwater reaction vessel. The results demonstrate that these layered nanohybrid sheets are robust and catalytically effective for green, H_2O_2-based micro-AUV propulsion where the storage and handling of highly explosive, toxic fuels are prohibitive due to size-requirements, cost limitations, and close person-to-machine contact.

KEYWORDS: *nanowires, platinum, cellulose, propulsion, hydrogen peroxide, autonomous underwater vehicles (AUVs)*
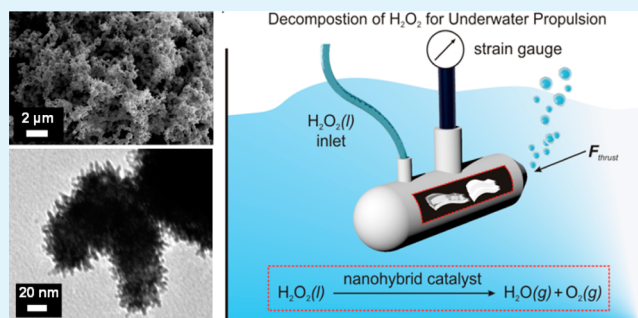
■ INTRODUCTION

Heightened interest in small scale maneuvering for autonomous underwater vehicles (AUVs) has driven the need to find propeller-free propulsion systems that are lightweight, environmentally friendly, and well-suited for small motion corrections.[1−3] Propeller-based AUVs are effective for constant speed motion but fail to provide small, controlled thrust (especially when the movement needed requires less than a full shaft rotation of the propeller) that can lead to degraded control precision, periodic oscillations of the vehicle's position, and inability to perform docking procedures that require quick propulsive bursts.[4] Pulsatile jet propulsion can assist in hovering/loitering, docking maneuvers, and provide the propulsive bursts necessary for maneuvering short-mission (<1 h) micro-AUVs, meaning AUVs on the length scale of half a meter down to a few centimeters. In terms of maximum power density, monopropellant and cold gas thrusters well outperform other modes of small scale vehicular propulsion including bipropellant rockets, air-breathing engines, and those powered by supercapacitors, thermal batteries, and Ni−Cd or Ag−Zn batteries.[5]

The monopropellant H_2O_2 is a green fuel (i.e., exhausting only oxygen and water, though carbon emissions may be generated during fuel production) that exhibits, when highly concentrated (i.e., 98% w/w), a significantly higher specific impulse than cold gas thrusters.[5−7] H_2O_2-based propulsion systems are also highly scalable and have been used on the micro/nanoscale within a wide variety of applications[8,9] and configurations that include platinum-loaded stomatocytes;[10] platinum and catalase conical-shaped or tubular bubble thrusters;[11−18] chemotaxis-driven silica-manganese "matchstick" particles and bimetallic nanorods;[19−23] catalytic janus motors,[24−28] and microelectromechanical systems (MEMS) based thrusters.[29,30] Furthermore, rocket grade H_2O_2 (80−98% w/w), typically utilized in rocket propulsion systems,[5−7] requires costly fabrication and storage measures and holds explosive dangers that are restrictive for some micro-AUVs where size-requirements, cost limitations, and close person-to-machine contact are especially problematic for storage and handling. Therefore, in this work, we seek to develop an efficient, cost-effective catalyst for reagent grade (30% w/w) H_2O_2 decomposition that supplies sufficient propulsion for
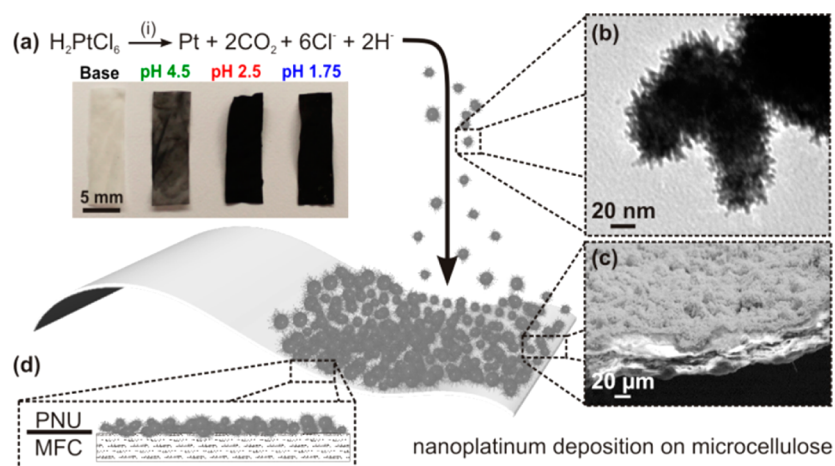
Figure 1. Schematic of the deposition of platinum nanourchins (PNUs) onto microfibrilated cellulose (MFC) films via reduction of chloroplatinic acid (H_2PtCl_6) with formic acid (HCOOH). (a, i) The reduction of H_2PtCl_6 proceeds as described in the text. (b) TEM and (c) SEM micrographs show the individual platinum nanoparticles and the resultant porous coating, respectively. (d) Cross-sectional schematic showing PNUs deposited onto MFC films. Not drawn to scale.

short-term micro-AUV missions. To achieve this goal we develop a Pt-based organic−inorganic nanohyrbrid that acts as a recyclable, durable, and noncolloidal catalyst (facilitating insertion/removal into a reaction chamber) for use in a wide variety of reaction chamber shapes and sizes.

Organic−inorganic nanohybrids are an emerging class of multifunctional materials with great potential for environmental and sustainable energy applications.[31,32] Of recent interest has been the generation of metallic nanostructures for optimizing catalytic activity;[33] however, sufficient carriage and dispersion of the catalytic particles throughout the reaction chamber is generally difficult.[34] Accordingly, nanohybrid materials provide a support medium for the active catalyst, in which a thin layer of functional nanocatalyst is maintained and dispersed at the surface of the carrier substrate. These nanohybrids offer ready access to a large surface area of the active compound as well as to interfaces, through which charge and energy transfer processes create new synergistic functions.

Catalytic nanohybrid materials are set to replace traditional metal-ceramic support catalysts because nanohybrid catalysts are heterogeneous catalysts with a higher surface area that increase catalytic activity, and unlike unbound, catalytic metal nanoparticles the incorporation of a support material helps reduce the loss of catalytic nanoparticles during the reaction as immobilized particles are less likely to be exhausted from the reaction chamber during violent exothermic reactions. Therefore, immobilized nanoparticles may help maintain catalytic efficiency over repeated use. Nanohybrid catalysts are being explored as components of organic redox[35] and C−C coupling reactions, as well as being explored for potential uses in alternative fuel generation.[36−39] Of the traditional metal-ceramic catalysts, platinum-based systems are one of the most widely used. The specific activity of platinum as a catalyst is dependent on the sequence of crystal planes the substrate encounters. An enlargement of surface area can be achieved by the decrease of particle size as well as the formation of porous structure, and recent efforts have made strides in the development of both nanostructured and porous platinum materials.[40−43] Nonetheless, Pt-nanoparticles with a large surface area are likely to agglomerate with repeated use, so to circumvent this problem Pt-nanoparticles are immobilized on a solid 2-dimensional support and arrayed in the third dimension.

At present, several efforts have resulted in immobilizing Pt nanoparticles onto surfaces comprised of carbon nanotubes,[44−46] graphene,[47,48] and silica,[49,50] for example. In order to excel as a viable catalytic material, Pt nanoparticles immobilized onto such substrates must display several important characteristics: (1) a high proportion of the [111] face and a tight size distribution, (2) a uniform and porous distribution across the support substrate, and (3) even in high metal loadings, high surface areas; all of which are important for optimizing the use of Pt as a monopropellant catalyst.[51,52]

Herein, we demonstrate the one-pot synthesis of platinum "nanourchins" (PNUs) and the subsequent fabrication of a green nanohybrid catalytic substrate, by synthesizing PNUs that upon nucleation begin to seed and generate a porous nano-Pt substrate on top of microfibrilated cellulose (MFC) substrates to form a PNU-MFC nanohybrid material. This process is shown to be a template-free route to microporous Pt catalysts, and the resultant morphology facilitates reduced activation energy for catalysis. These unique features result in reducing the activation energy for the catalytic conversion of H_2O_2 to oxygen and water; moreover, we utilize this platinum-cellulose hybrid material to demonstrate the possibility of H_2O_2 conversion as a viable, green energy source for the propulsion of underwater vehicles.

■ RESULTS AND DISCUSSION

Synthesis of Pt-Nanourchins and Nanostructured Pt-Papers. PNUs can be synthesized from a template-free route at room temperature via the reduction of hexachloroplatinic acid (H_2PtCl_6) by formic acid (HCOOH). PNUs were loaded in situ on MCFs to form the catalytic Pt-papers. PNU loading was performed by placing MFC films within 11.6 mM chloroplatinic acid solution (33% Pt-to-cellulose weight percentage), adding 10% formic acid, and adjusting the solution pH with ammonium hydroxide (Figure 1 and Experimental). The formic acid (HCOOH) reductant reacts with chloroplatinic acid (H_2PtCl_6) in the following manner (eqs 1−3).[53]

$$H_2PtCl_6 \rightarrow 2H^+ + PtCl_6^{2-} \tag{1}$$

$$2HCOOH \rightarrow 2H^+ + 2COOH^- \tag{2}$$
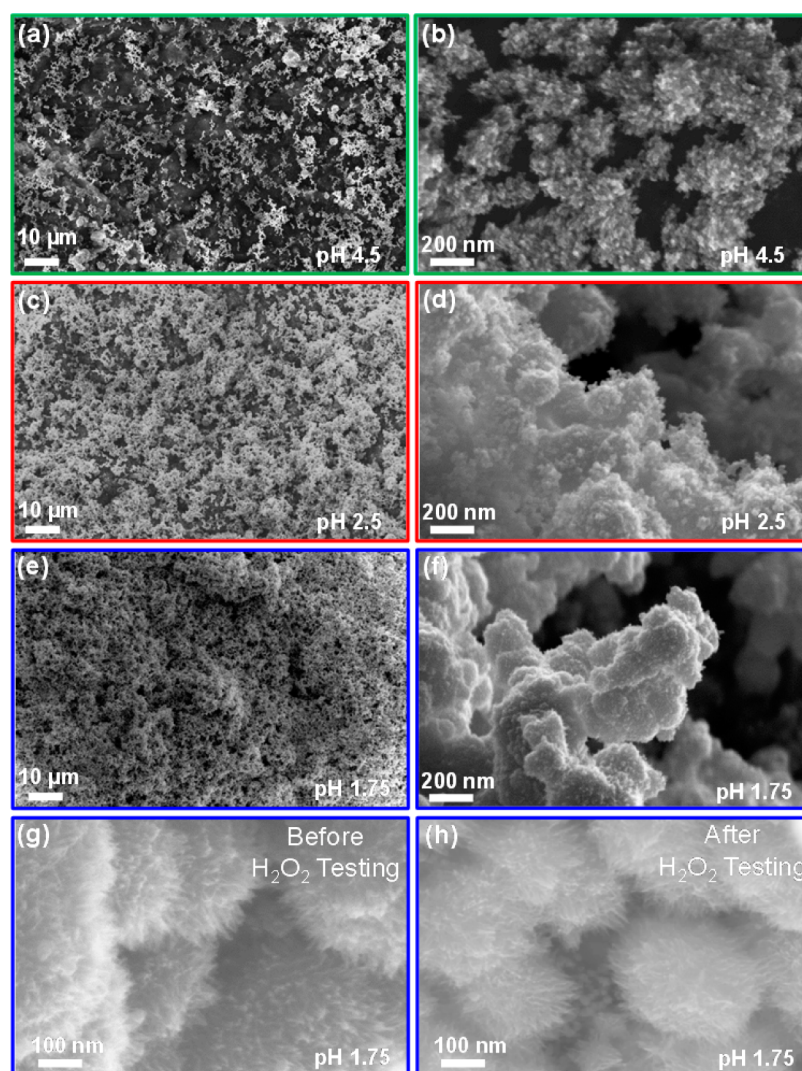
Figure 2. Scanning electron microscopy images obtained at 20 keV show the size, density, and morphology of PNUs deposited on MFCs with a pH of 4.5 (a-b, green), 2.5 (c-d, red), and 1.75 (e-f, blue) at magnification of 1 kx (left column) and 60 kx (right column). High magnification (150 kx) SEMs (g, h, blue) illustrates Pt nanowire (3−5 nm dia.) growth during PNU deposition at pH 1.75 before (g) and after (h) H_2O_2 testing.

$$PtCl_6^{2-} + 2COOH^- \rightarrow Pt + 2CO_2 + 6Cl^- + 2H^+ \qquad (3)$$
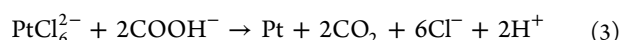
The velocity of this PNU growth mechanism is increased in more basic environments as proton generation ($2H^+$) occurs within each of the three sequential reactions (eqs 1 − 3). Therefore, in more acidic environments the increased presence of H^+ hinders reaction progression leading to a higher density deposition of finely nanostructured PNUs, while the presence of OH^- in more basic environments conversely leads to a lower density deposition of PNUs even though the initial molarity of choloroplatinic acid solution is the same.

SEM and TEM Characterization. The effects of pH on the PNU growth mechanism are readily apparent in the distinct size, density, and morphology of the PNUs deposited on MFC at pH 1.75, 2.5, and 4.5 (Figure 2). The density of the PNU clusters is significantly enhanced as deposition pH decreases. The SEM images in Figure 2 illustrate this disparity in density as the cellulose background (black) is readily apparent against the bright PNUs when the deposition pH is set to 4.5, while no cellulose background is visible when a deposition pH of 1.75 is utilized. Likewise, the morphology of the deposited PNUs changes from rough particles with 10−30 nm jagged edges at

pH 4.5 deposition to a surface with highly dense nanospikes with diameter of 3−5 nm at pH 1.75 deposition (Figure 2 and Figure 3). These highly dense, PNUs (pH 1.75) form tall (~10 μM, Figure 1c) coral-like structures on the surface of the MFC that are retained after extensive testing (Video S1, Figure 2h, and Figure S1). High-resolution transmission electron microscopy (HRTEM) reveals (111) planes with lattice spacing of 0.23 nm (Figure 3). These nanowires do not form with a preferential crystallographic direction as (111) planes are seen to be oriented in different directions with respect to the nanowire axis, even for different regions of the same sample (*e.g.* regions a and b in Figure 3). Therefore, PNU growth is fractal in nature.

Research groups have used similar techniques to produce single-crystal Pt nanowires on carbon powder/nano-spheres,[53,54] carbon nanotubes,[55] and graphene.[56] We build upon these works by not only growing the template-free Pt nanowires on a different, biocompatible substrate (i.e., cellulose) but also by changing the overall morphology of the deposited structures to create a thick film of coral-like microstructures that are arrayed in three dimensions and coated with urchin-like nanowires. These thick extremely high
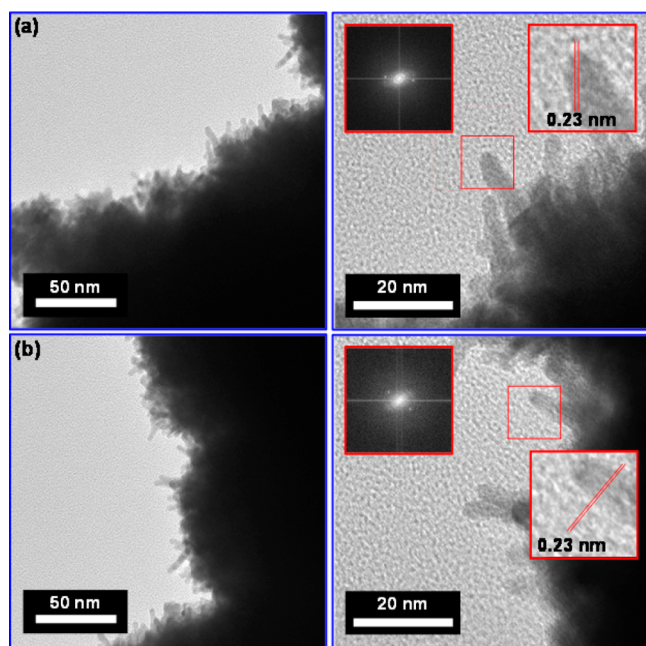
Figure 3. Regions (a) and (b), imaged by TEM, displaying Pt nanowires acquired from PNUs deposited onto MFC films at pH 1.75 (blue). The left column displays images recorded at 100 kx, while the right column shows 300 kx HRTEM images of the same region. The outlined region (red box) is used to generate the FFT diffraction pattern (inset) and is further magnified (other inset) to show (111) interplanar spacing (red lines) at 0.23 nm intervals.

surface area Pt micro/nanostructures were created by utilizing a high H_2PtCl_6 (11.6 mM) growth molarity in conjunction with low pH (1.75) and low temperature (25 °C). Low pH environments have shown to decrease the conductivity of the hexachloroplatinic acid/formic acid solution which subsequently slows the reaction time.[53] This phenomenon was apparent in our work as reaction times (i.e., the time for the Pt salt solution to transition from a yellow to clear color and PNU to MFC deposition to occur, see Experimental) varied from 30 min, 10 h, and 16 h for solutions held at pH 4.5, 2.5, and 1.75, respectively. Likewise, research reports have shown that elevated temperatures (e.g., 70 °C) accelerate colloidal Pt

deposition reactions to create more spherical nanostructures, while low temperature reactions held at room temperature form nanospikes or nanowires that agglomerate into larger particles due in part to dipole−dipole interactions.[56−58] Thus, by slowing the Pt reduction reaction time via low pH and low temperature environments, anisotropic growth of Pt crystal growth is favored on the surface of Pt(111), as for face centered crystal structures, the order of surface energies is (111) < (100) < (110).[59−61] High molar concentrations with high platinum-to-carbon weight ratios (≥30%) enhance the density of nanowire growth,[54] and in our experience with cellulose, the overall thickness of the PNU film. Furthermore, such a thick, macroporous Pt film nanostructured with Pt nanowires vastly enhances the surface area of the underlying MFC substructure and also provides additional strength and rigidity needed for the subsequent highly violent and exothermic H_2O_2 decomposition reactions.

Elemental and Surface Area Analysis. X-ray photoelectron spectroscopy (XPS) elucidates the elemental characteristics of the deposited PNUs, while isothermal gas adsorption and electrochemical analysis illustrate their relative surface area/density. PNU-MFC samples prepared at pH 1.75, 2.5, and 4.5 exhibit nearly identical XPS core line spectra (Figure 4 and Table S1). The deconvolution of the Pt 4f doublet reveals the presence of three components, assigned to metallic Pt (71.0 ± 0.5 eV), PtO (+0.8 eV), and PtO_2 (+2.0 eV) with intensity percentages of 58.3% ± 4.7%, 21% ± 2.0%, and 20.7% ± 3.5%, respectively. Importantly, XPS measurements of Pt film evaporated (∼150 nm thick) onto the MFC revealed nearly identical binding energies (BEs) for the Pt 4f components with comparable intensity percentages: Pt (51%), PtO (32%), and PtO_2 (17%). Similarly, the oxygen 1s core level spectrum can be deconvolved into two components assigned to physisorbed (532.9 eV) and Pt-bound (−1.5 eV) oxygen species (Figure 4 and Table S2). The XPS analysis of PNU samples and evaporated Pt films is consistent with the previously reported XPS work using thermally cracked atomic oxygen on Pt(111) and thin film oxides of Pt grown on Si/SiO_2 wafers.[62,63] Subsequently this XPS analysis demonstrates that the chloroplatinic acid chemical reduction process is effective at depositing metallic Pt onto cellulose as it deposits nearly
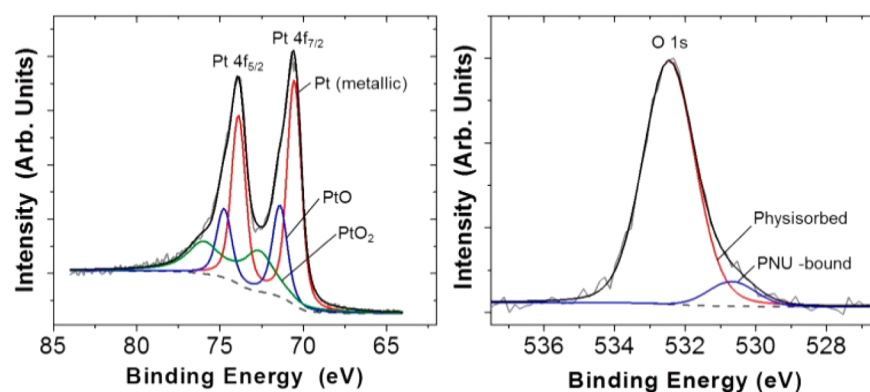
Figure 4. (Left) Pt 4f core line spectrum of an MCP sample fitted to three Voigt doublets (solid line) and superimposed on a Shirley-type background function (dashed line). Spin−orbit intensity ratio of the Pt $4f_{7/2}$ and Pt $4f_{5/2}$ components was set to 0.75, and the spin−orbit splitting was kept at 3.3 eV. The binding energy of the metallic $4f_{7/2}$ component was found to be 71.0 ± 0.5 eV. (Right) O 1s core line spectrum of an MCP sample fitted to two Voigt singlets (solid line) and superimposed on a Shirley-type background function (dashed line). The binding energy (BE) of the higher BE component (physisorbed oxygen) was found to be 532.9 ± 0.5 eV, while the low BE component (PNU-bound species) exhibited a positive 1.5 eV chemical sift.
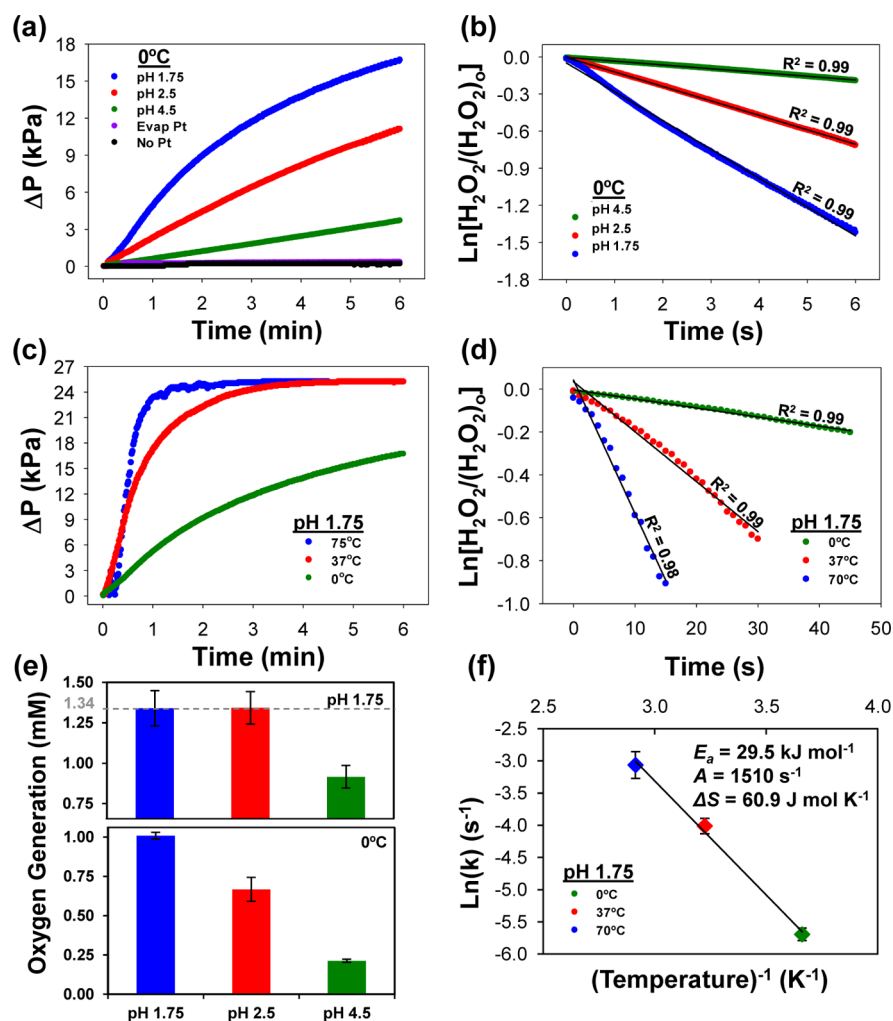
Figure 5. O_2 evolution during H_2O_2 decomposition. Differential pressure plots (O_2 generation of test versus control flask, see Methods) for (a) PNU-MFC [pH 1.75 (blue), pH 2.5 (red), pH 4.5 (green)] and control samples [Pt (purple), and no Pt (black)] evaporated held at constant temperature (0 °C) with (b) corresponding first-order fit of H_2O_2 decomposition for PNU-MFC samples and for (c) pH 1.75 PNU-MFC samples held at varying temperatures [70 °C (blue), 37 °C (red), and 0 °C (green)] with (d) corresponding first-order fit of H_2O_2 decomposition. (e) Total O_2 generation from 1.34 mM maximum possible (gray dotted line) during H_2O_2 decomposition for (bottom) PNU-MFC samples [pH 1.75 (blue), pH 2.5 (red), and pH 4.5 (green)] held at constant temperature (0 °C) and (top) pH 1.75 PNU-MFC samples held at varying temperatures [70 °C (blue), 37 °C (red), and 0 °C (green)]. (f) Arrhenius plot (natural logarithm of the Arrhenius equation) for the pH 1.75 PNU-MFC sample acquired at three temperature points [70 °C (blue), 37 °C (red), and 0 °C (green)]. Error bars represent one standard deviation from the mean (n = 3).

identical Pt, PtO, and PtO_2 percentages on cellulose as high-vacuum evaporation of pure Pt.

N_2 adsorption was attempted to characterize the surface area and porosity of all of the distinct PNU-MCF samples (Figure S2). The bare MCF substrate did not yield a measurable nitrogen adsorption isotherm and neither did PNU-MCFs prepared at pH 2.5 and 4.5 (data not shown). Even with visible Pt coverage, the cellulose substrate dominated the mass of the hybrid material (PNU-MFC grown at pH 2.5 and 4.5) and defeated the utility of this gas adsorption technique. However, PNUs deposited at pH 1.75 on MCF did yield a measurable adsorption isotherm, with a Brunauer–Emmett–Teller (BET) surface area of 1.8 m^2/g and total pore volume of 1.6×10^{-3} cm^3/g (Figure S2). The isotherm appeared to be type II in its shape, consistent with a macroporous material. Likewise ferricyanide cyclic voltammetry reveals a noticeable current response for pH 1.75 prepared PNU-MFC samples and negligible responses for those prepared at pH 2.5 and 4.5

(Figure S3). Such electrochemical experiments qualitatively demonstrate that the deposited Pt nano/microcrystal structures of the pH 1.75 samples become sufficiently large/dense to conduct electrons heterogeneously from solution and between Pt architectures—bypassing the cellulose insulator. Thus, N_2 adsorption and electrochemical experiments reveal that PNU deposited on MFC films at a pH 1.75 have a dense, high surface area nature—traits that are well-suited for H_2O_2 decomposition catalysis.

Catalyst Characterization: H_2O_2 Decomposition. The catalytic nature of the PNU-MFC catalysts was monitored via H_2O_2 decomposition testing. H_2O_2 decomposition testing was performed for all 3 PNU-MFC samples (i.e., pH 1.75, 2.5, and 4.5, respectively) as well as for 2 control samples (i.e., MFC with evaporated platinum (150 nm) and MFC without Pt) (Figure 5a and Video S2). Two round-bottom flasks [one containing the test sample (test flask) and the other not (control flask)] were tested in parallel within an ice bath (0 °C/

273 K) to monitor differential pressure between the test and control flasks (see the Experimental Section, Figure S7). The differential pressure increase between the test and control flasks is monitored on a laptop computer via a manometer for 6 min per experiment. To begin the experiment, H_2O_2 is injected within both the test and control flasks, while a magnetic stir bar mixes the solutions to ensure fuel/catalyst interaction. A lower H_2O_2 concentration (3% w/w in H_2O) is used during differential pressure experiments to ensure that no steam is produced during the reaction and hence all generated pressure is due to oxygen generation via direct H_2O_2 decomposition (eq 4).
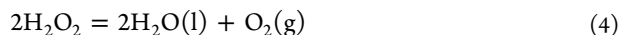
$$2H_2O_2 = 2H_2O(l) + O_2(g) \tag{4}$$

Figure 5a portrays the resultant pressure curves from O_2 evolution during differential pressure experiments (0 °C) associated with the three distinct PNU-MFC samples [pH 1.75 (blue) > pH 2.5 (red) > pH 4.5 (green)] and from two distinct control samples where a bare MFC strip (black) is one and a MFC strip with planar evaporated Pt (purple) is the other. The pressure curves progressively increase in slope/magnitude as the Pt particle density and nanostructuring increases (i.e., pH 1.75 > pH 2.5 > pH > 4.5), while negligible pressure responses are recorded for the two control samples. Differential pressure is converted into moles of oxygen via the ideal gas law ($PV = nRT$) where P is differential pressure (Pa), V is total volume of the test flask after insertion of septa (0.123 L), n is moles of generated oxygen, R is the universal gas constant (8.314 J mol^{-1} K^{-1}), and T is temperature (273 K) (Figure 5e). The PNU-MFC sample fabricated at pH 1.75 generates the most moles of oxygen (~1 mM) out of a total possibility of 1.34 mM per 3% H_2O_2 when reaction temperature is held constant at 0 °C (Figure 5e, bottom). The rate of H_2O_2 decomposition can be subsequently obtained by converting generated moles of O_2 to moles of H_2O_2 via the reaction stoichiometry, viz., 2 mol of H_2O_2 consumed for every 1 mol of O_2 generated. The kinetics of H_2O_2 over the distinct PNU-MFC samples can be described by the following first-order rate equation[64]

$$\ln\left(\frac{[H_2O_2]}{[H_2O_2]_o}\right) = -k_{obs}t \tag{5}$$

where k_{obs} represents an apparent kinetic constant; k_{obs} represents the absolute value of the slope of the graph of the natural logarithm of H_2O_2 concentration versus time (Figure 5b). The k_{obs} values for the 3 distinct PNU-MFC samples (held at 0 °C) are as follows: 3.2 ± 0.1 s^{-1} (pH 1.75), 1.7 ± 0.2 s^{-1} (pH 2.5), and 0.4 ± 0.1 s^{-1} (pH 4.5) where the number of repeated experiments for each sample is three (i.e., $n = 3$) and ± error represents one standard deviation from the mean.

Next, the apparent activation energy (E_a) of H_2O_2 decomposition was calculated for the pH 1.75 sample, the most effective PNU-MFC catalyst, through the use of the Arrhenius equation which correlates the observed reaction rate constant (k_{obs}) with absolute temperature (K)

$$k_{obs} = Ae^{-E_a/RT} \tag{6}$$

where A is the pre-exponential factor, E_a is the activation energy, and R is once again the universal gas constant. By following the Freidman method,[65] the activation energy can be found by plotting the natural logarithm of the Arrhenius equation

$$\ln(k) = \frac{-E_a}{R}\frac{1}{T} + \ln(A) \tag{7}$$

where $-E_a/R$ represents the slope of the plot. The pH 1.75 PNU-MFC sample was subsequently tested at three distinct temperatures (i.e., 0 °C, 37 °C, and 70 °C) (Figure 5c), the respective reaction rates (k_{obs}) were extracted from plotting the first-order fit of H_2O_2 decomposition (Figure 5d, Table 1). The

Table 1. H_2O_2 Decomposition Kinetics for PNU-MFC (pH 1.75)

temp (K)	k_{obs} (s^{-1} × 10^{-3})	E_a (kJ mol^{-1})	A (s^{-1})	ΔS (J mol^{-1} K^{-1})
273	3.2 ± 0.1	29.5	1510	60.9
310	18.1 ± 2.1			
343	46.7 ± 9.1			

pre-exponential factor (A), entropy of activation ($\Delta S = \ln(A) \times R$), and E_a were acquired from plotting the logarithm of the Arrhenius equation (Figure 5f, Table 1). Table 2 portrays the

**Table 2. H_2O_2 Kinetics of Noncolloidal Nanostructured and Conventional Catalysts at Low Temperature (~25 °C)^a**

Catalyst	k_{obs} (s^{-1} × 10^{-3})	E_a (kJ mol^{-1})	Ref.
AuNPs on Graphene	3.9 − 5.7	20.4	[66]
Graphene	3.2 − 3.4	28.8	[67]
PNU-MFC (pH 1.75)	**3.2 − 4.5**	**29.5**	*
Pt/Pd NPs (3:1) on Nafion	5.4	34.0	[68]
Pt/Pd NPs (1:4) on Nafion	4.5	36.3	[68]
Ferrihydrates	0.1 − 0.3	59.4†	[69]
Iron Oxide	0.5 − 4.7	60.0	[70]
Pyrite	0.03 − 0.1	79.5	[71]

^{a}Legend: AuNPs = gold nanoparticles; PNU = platinum nanourchins; MFC = microfibrilated cellulose; NPs = nanoparticles. ^{b}Results presented in this work. ^{c}Lowest E_a value reported in manuscript.

k_{obs} and activation energy of the PNU-MFC catalysts (fabricated at pH 1.75, blue) as compared to both nanostructured and conventional catalysts used in H_2O_2 decomposition that are noncolloidal in nature, meaning they are attached to macro-sized surfaces. The PNU-MFC samples have the ability to lower activation energy for H_2O_2 decomposition by approximately 50−63% over conventional materials (i.e., ferrihydrates, iron oxide, and pyrite) and by 13−19% for similar nanostructured surfaces (i.e., Nafion substrate peppered with Pt/Pd nanoparticles). Recent reports of catalysts based upon few-layer graphene, significantly more costly and time-consuming to produce than MFC, show minimal decrease (2.4%) in activation energy as compared to the PNU-MFC (pH 1.75) strip while further modification with AuNPs demonstrates a 44% comparative decrease in E_a.

Micro-AUV Propulsion. The ability of the PNU-MFC (pH 1.75) catalyst to produce propulsive thrust was evaluated by developing a test platform that simulated a micro-AUV, inserting 10 PNU-MFC strips into the reaction chamber (which is approximately 15% of the total volume of the reaction chamber), and fixing the vehicle to a strain gauge mounted to an experimental water tank (see Figure 6, Videos S3−S5, and Experimental). The average mass flow rate of fuel ($\dot{m}$) [30% H_2O_2 w/w as noted by manufacturer, with 30% of fuel assumed to have a density of 1.4 g cm^{-3} (H_2O_2) and 70% of fuel

17842

dx.doi.org/10.1021/am504525e | ACS Appl. Mater. Interfaces 2014, 6, 17837−17847
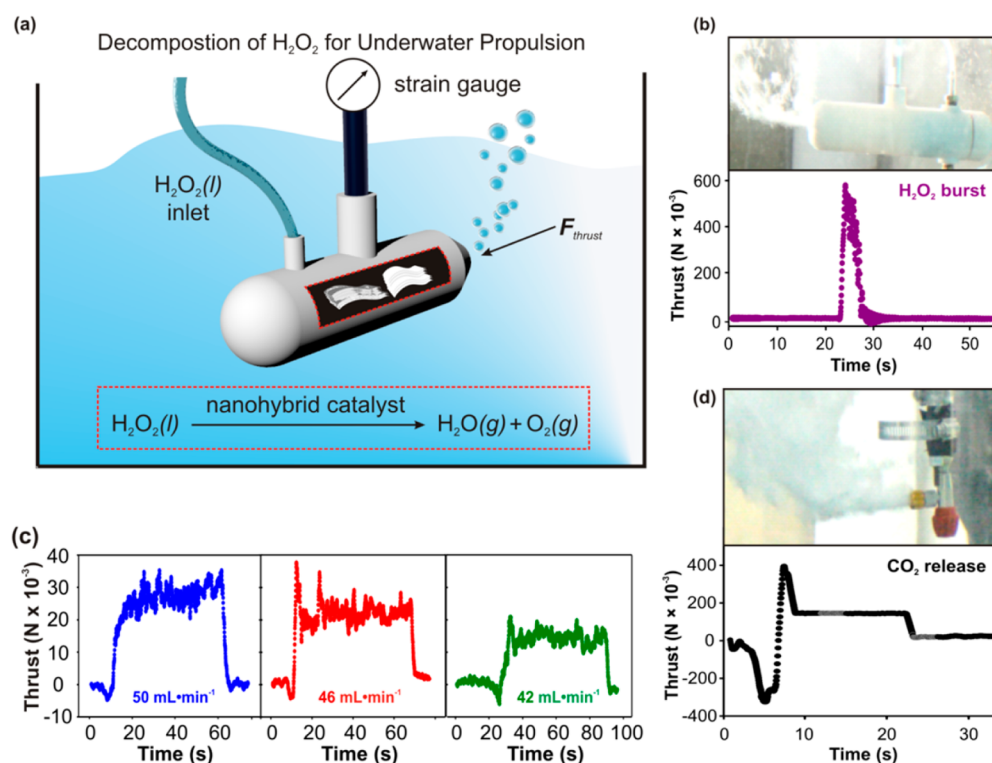
Figure 6. Underwater testing of bubble propellant from H_2O_2 conversion to steam and oxygen. (a) Schematic of the reaction vessel/rocket illustrating the packing of the PNU hybrids within the chamber, introduction of H_2O_2, exodus of generated gas to produce thrust, and thrust measurement via a torque transducer. (b) Instantaneous release of H_2O_2 (5 mL of 30% w/w) into the reaction chamber resulted in a maximum burst thrust of approximately 0.6 N, sustained over 10.5 s. (c) Sustained release of H_2O_2 (5 mL of 30% w/w) into the reaction chamber generated thrusts of approximated 0.02−0.03 N over 60 s. (d) Release of compressed CO_2 from a 20 mL CO_2 cartridge revealed a sustained thrust that was four times less powerful than the H_2O_2 burst (~0.15 N) for 13.5 s.

assumed to have a density of 1.0 g cm³ (H_2O)] was calculated for five test scenarios: three steady flow environments (Figure 6c) where fuel is pumped into the reaction chamber at approximate flow rates of 50 mL min⁻¹ (blue), 46 mL min⁻¹ (red), and 42 mL min⁻¹ (green) via a syringe pump; one bursting environment (purple) where 5 mL of fuel was rapidly injected into the reaction chamber by applying manual pressure (Figure 6b and Video S3); and finally, as a comparative control, cold gas propulsion from the pressure release of a 16 g CO_2 cartridge (Figure 6d and Video S4). Also a control experiment was carried out by pumping 10 mL of H_2O into the reaction chamber of the micro-AUV, which, subsequently, produced negligible thrust (Video S5). Specific impulse, the thrust per unit mass flow rate of propellant, can be defined as

$$I_{sp} = \frac{T}{\dot{m}} \tag{8}$$

where T is the thrust, and ($\dot{m}$) is the mass flow rate. As the H_2O_2 flow rate increases from 0.78 g s⁻¹ (42 mL min⁻¹), to 0.86 g s⁻¹ (46 mL min⁻¹), and finally to 0.93 g s⁻¹ (50 mL min⁻¹) the thrust proportionally increases—yielding an increasing specific pulse (Table 3). The specific impulse for the burst of H_2O_2 reached a value of approximately 205 m s⁻¹, nearly a 70% increase over the CO_2 cartridge. The total impulse ($I_{tot} = T * t$) for each test scenario was subsequently calculated over the amount of elapsed time (t) for 20 mL of fuel usage which is also the volume of the CO_2 cartridge. Thus, by bursting 20 mL of reagent grade H_2O_2 fuel, one can expect more than double the total impulse achieved from releasing 20 mL of compressed CO_2 (Table 3).

Table 3. H_2O_2 Propulsion Characteristics for Test Micro-AUV[a]

Flow Type	$\dot{m}$ (g s⁻¹)	I_{sp} (m s⁻¹)	I_{Tot} (kJ mol⁻¹)	V (m s⁻¹)	P_D (kW m⁻³)
	0.78	18.6	0.42	0.87	0.63
Steady	0.86	25.4	0.58	1.07	1.18
	0.93	30.0	0.67	1.20	1.69
Burst	1.18	205	4.58	4.76	104
CO_2	2.13	122	1.95	2.73	19.7

[a]Color scheme matches graphical plots in Figure 6.

The average velocity for the micro-AUV can also be estimated from the following equating steady-state thrust/drag equation

$$v = \sqrt{\frac{2T}{C_D \rho A}} \tag{9}$$

where C_D (0.04) is the drag coefficient for a hemispherical nose and a cylindrical body with a diameter to length ratio of 1:6 (a shape and aspect ratio similar to the test micro-AUV),[72] ρ is the density of surrounding fluid (H_2O), T is the generated thrust, and A is the cross-sectional area of the micro-AUV (9.65 cm²). From these average velocity calculations, the amount of power per unit volume or power density ($P_D = T*v$) reveals a 5-fold increase in the P_D for the bursting reagent grade H_2O_2 fuel (104 kW m⁻³) as compared to the CO_2 cartridge release (19.7 kW m⁻³) (Table 3).

■ CONCLUSION

PNUs can be grown from MFC films through a facile one-pot, chemical synthesis process in which strips of MFC are placed within a chloroplatinic acid solution and formic acid is introduced as a reductant. The size, density, and morphology of deposited PNUs can be altered by adjusting the speed of the reaction through manipulation of the solution pH with ammonium hydroxide. Chloroplatinic deposition solutions held at higher pH values (pH 4.5) grow low-density, rough PNUs with 10−30 nm jagged edges. Lower pH deposition values (pH 1.75) grew high-density, highly nanostructured PNUs with thin nanospikes (diameter 3−5 nm) that build upon each other to form macro/micro, coral-like structures that extend 10 μM in height. To our knowledge, thick macro/microporous films of PNUs have never been deposited on bioderived substrates. Although nanohybrid catalysts composed of needle-like Pt-networks have been prepared on micro/nanostructures,[53−56] the PNU-MFC nanohybrid catalysts developed herein offers a robust platform that can be employed under stressed reaction conditions, in which a basic nanoparticle catalyst would not survive.

The catalytic nature of these PNU-MFC inorganic−organic nanohybrid materials during H_2O_2 decomposition is significant. The PNU-MFC structures reduce the activation energy (E_a) of H_2O_2 decomposition by 50−63% over conventional materials (i.e., ferrihydrates, iron oxide, and pyrite)[69−71] and by 13−19% for similar nanostructured surfaces (i.e., Nafion substrate peppered with Pt/Pd nanoparticles)[68] and are on par with expensive few-layer graphene substrates.[66] In terms of micro-AUV propulsion, 10 PNU-MFC strips situated within a small (20 mL) reaction chamber, where only ∼15% total volume of the reaction chamber is utilized, can deliver approximately 0.6 N of bursting thrust from reagent grade (30% w/w) H_2O_2 which correlates to a 5-fold increase in the power density (P_D) over a similar sized cold gas thruster (i.e., venting compressed gas from a 16 g CO_2 cartridge, that contains an approximate volume of 20 cm^3 and approximate pressure of 45 MPa/6.5 kpsi at 22 °C). Therefore, propulsion with 30% H_2O_2 could propel the micro-AUV with an average velocity of 4.8 m/s and a distance of approximately 50 m with 20 mL of fuel (i.e., the amount of fuel that currently can be carried on-board the test device/vehicle) as compared to the 20 mL of compressed CO_2 that could propel the micro-AUV with an average velocity of 2.7 m/s and a distance of approximately 37 m. This bursting thrust is within the milli-Newton thrust range needed for attitude adjustment with micro/nanosatellites and micro-AUV propulsion for forward movement, hovering/loitering, or docking maneuvers.[7,73,74] Therefore, an H_2O_2-based propulsion system, with PNU-MFC catalysts, offers a relative inexpensive, simple (no mechanical parts such as propellers), and recyclable solution to micro-AUV propulsion.

The use of cellulose provides various functions including but not necessarily limited to catalyst recyclability as paper can be dissolved and platinum recovered, low-cost due to its ubiquitous nature in the environment, and nontoxicity as cellulose can degrade without harm to the environment. The chemical deposition of Pt nanourchins on paper-based substrates eliminates the need for electroplating or substrate conditioning and therefore provides a catalyst fabrication route that could be scaled-up for large-scale manufacturing. Furthermore, this technology offers a potentially less expensive version to conventional microgas turbines as well as thrusting

capabilities that could be positioned for faster vehicle turns than propeller-based propulsion systems. We see use of such inexpensive H_2O_2-based propulsion systems to enhance existing micro-AUV propulsion systems and/or to act as a stand-alone propulsion system for single-use micro-AUVs that can be discarded without retrieval for myriad applications such as underwater chemical sensing to payload delivery. Of course such Pt-cellulose would not be appropriate for larger vehicle/rocketry which require higher concentrations of hydrogen peroxide (e.g., rocket grade H_2O_2) and mass flow rates which could substantially degrade the Pt-cellulose catalyst. In future work, we hope to optimize the size/shape of the reaction chamber, volume of catalyst (as 10 PNU-MFC strips equates to only ∼15% total volume of the reaction chamber), and exhaust nozzle to improve both the efficiency of H_2O_2 decomposition via the PNU-MFC catalyst and maximize the thrust output of the propulsion system. Furthermore, the size of the reaction chamber and on-board fuel capacity will be optimized for particular time durations required for specific underwater propulsion applications.

■ METHODS

Microfibrillated Cellulose (MFC) Film Fabrication. Microfibril cellulose was purchased from the University of Maine Process Development Center (Orono, ME) as a 3% (w/w) aqueous slurry. MFC films were prepared by vacuum filtration of a 10:1 slurry:water mixture through a 0.2 μm nylon filter. The deposited cake was removed from the filter and pressed between glass plates to dry under vacuum at 75 °C. The resultant supports were of uniform composition and thickness (ca. 50 μm). The fabricated MFC was cut into strips approximately 1.9 cm × 0.65 cm by a 40W Epilog Laser Mini printer and weighed via a high resolution (±0.01 mg) laboratory balance.

Platinum Nanourchin (PNU) Growth on MFC Film. The stock solution for platinum "nanourchin" (PNU) growth was created by adding 360 mg of chloroplatinic hexahydrate (37.5% Pt, Sigma-Aldrich 206083) to 54 mL of deionized (DI) H_2O and 6 mL of reagent grade formic acid (≥95%, Sigma-Aldrich F0507). The stock solution was divided into three equal 20 mL parts and poured into 3 distinct 40 mL Pyrex beakers. Drops of ammonium hydroxide were added to each of the 3 solutions to raise the pH from a base level of 1.55 to 1.75, 2.5, and 4.5, respectively. Three MFC strips were placed into each of the 3 beakers to create a Pt-cellulose ratio of 33% by weight in each pH environment where the average weight of three test strips was approximately 14.85 mg. The solutions were covered with Parafilm and left in a chemical hood until each solution turned from yellow to clear (∼30 min for pH 4.5, ∼10 h for pH 2.5, and ∼16 h. for pH 1.75)—signifying the termination of the reaction (Figure 7). After the reactions were complete the now PNU-MFC strips were washed thrice in DI water and allowed to air-dry before subsequent experimentation.

Platinum Evaporation on MFC Film. In order to create a planar Pt-MFC control sample, platinum was evaporated onto MFC strips. The MFC strips were taped onto a substrate holder with 1 mm thick Kapton tape and placed within the rotating carousel holder of a Temescal Model FC-2000 E-beam Evaporator. 50 nm of titanium was first evaporated onto the bare MFS strips at a rate of 0.1 nm/s to provide an adhesion layer for subsequent Pt evaporation (150 nm, at a rate of 0.1 nm/s).

H_2O_2 Decomposition. Two 100 mL round-bottom glass flasks are used to monitor oxygen generation from H_2O_2 decomposition. The flasks are sealed with rubber septa tops that are flanged with a sleeve-like extension that protrudes into and folds down over the neck of the vessel. Before septa insertion, magnetic stir bars are placed inside each flask, and a PNU-MFC sample is placed inside the test flask only. An Extech HD750 Differential Pressure Manometer (measuring up to ±5 psi/34.5 kPa) is connected to the flask via two high strength silicone tubes (dia.: 0.375 in./9.525 mm) that fit over each of the two barbed manometer fittings on one end and over the barbed plastic couplers
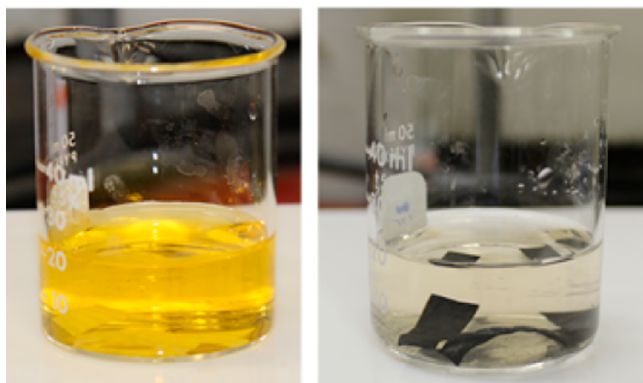
Figure 7. Chloroplatinic deposition solution color change from an initial yellow color (left) to a final clear/gray (right) color when the reaction is complete. (left) Three MFC samples start as white in color and then (right) appear black in color when the reaction is complete.

connecting to syringe needles on the opposite end. The syringe needles (coupled to the manometer via the plastic tubing) are inserted into the test and control round-bottom flasks separately by piercing through the diaphragm of the septa (Figure 8). In this arrangement,

Figure 8. Experimental setup for monitoring pressure from O_2 evolution during H_2O_2 decomposition accelerated by the PNU-MFC catalysts. (Left) Constant temperature water or ice bath holds working and control round-bottom flasks on a hot plate while (right) a differential pressure monitor measures pressure changes. A USB cord (silver) originating from the differential pressure monitor connects to a laptop monitor for data analysis.

the differential pressure between the test and control flasks can be measured by the manometer. The flasks are placed inside ice or water baths on top of magnetic stirrer hot plates to maintain isothermal conditions at 0 °C, 37 °C, and 70 °C, respectively. The H_2O_2 fuel (3% w/w in H_2O, diluted from 30% w/w in H_2O as noted from manufacturer: Fisher Scientific BP2633-500) placed within a 50 mL conical centrifuge tube is also immersed in the respective ice/water baths. Both the immersed flasks and H_2O_2 fuel are allowed to thermally equilibrate with the bath temperatures before experimentation. After thermal equilibration, a syringe needle is inserted and removed from each of the septa diaphragms to equilibrate pressure inside the flasks with the atmospheric pressure. The differential pressure, graphically displayed and monitored against time on a laptop computer via a universal serial bus (USB) connection, is zeroed before experimental runs so that subsequent changes in differential pressure accurately reflect pressure generated from oxygen generation. Finally, 3 mL of H_2O_2 (3% w/w in H_2O) is simultaneously injected into each

round-bottom flask, while the magnetic stir bars are run at 200 rpm to ensure catalyst/fuel mixing. Resultant differential pressure vs time data is collected for 6 min per experiment. Each experiment is carried out in triplicate ($n = 3$) with 3 distinct PNU-MFC samples and 3 control samples, *viz.*, PNU-MFC samples grown at pH 1.75, pH 2.5, and pH 4.5, respectively, as well as two control samples: a bare MFC film and a Pt-MFC film containing 150 nm of evaporated Pt.

Micro-AUV Fabrication and Testing. The micro-AUV was designed with computer aided design software (SolidWorks) and printed with an Objet500 Connex 3D printer with a PMMA like resin. The micro-AUV was then fitted to a 30.5 in. (0.77 m) rigid arm through screw thread fastening and submerged into a water tank (250 gallons of water in a tank with total volume capacity of 350 gallons). The opposite end of the arm was secured to a torque transducer (Interface model 5350-50:50 oz-in sensor) mounted above the water tank. The transducer reported torque measurements with 0.001 N-m precision along the parallel axis of the micro-AUV via a CPU connection. Force (thrust) measurements were calculated via software on the CPU. Reagent grade H_2O_2 was pumped into the reaction chamber via a 50 mL syringe connected to the reaction chamber via high strength silicone tube (dia.: 0.375 in./9.525 mm) that fits over a plastic barbed fitting. Steady flow rates were achieved by applying constant pressure to the syringe via a syringe pump, while bursting flow was achieved by applying manual pressure.

X-ray Photoelectron Spectroscopy (XPS). XPS analysis was performed using a Thermo Scientific K-Alpha XPS instrument with a monochromatic Al Kα source, and the spectral peaks of core levels were fitted using a commercial XPS analysis software by Unitfit. The fitted functional form was a set of Voigt doublets (Pt 4f) or singlets (O 1s), superimposed on a Shirley-type background function.

Surface Area Measurement. Nitrogen adsorption analysis was conducted with a Micromeritics ASAP 2010 system at 77 K (Micromeritics Instrument Corporation, Norcross, GA). Samples were degassed at 60 °C prior to analysis. Surface area was calculated by the Brunauer-Emmett-Telller (BET) method, pore size was measured by the Barrett−Joyner−Halenda (BJH) method using the adsorption branch of the isotherm, and total pore volume was determined by the single point method at relative pressure (P/P_0) 0.97.

Electrochemical Measurements. Cyclic voltammograms (CVs) were carried out within a 3-electrode setup where the PNU-MFC and MFC strips acted as the working electrode, Ag/AgCl (3 M KCL) as the reference electrodes, and a Pt wire as the auxiliary electrode. The 3 electrodes were submerged within 20 mL of 20 mM Fe(CN)$^{4-}_6$ and 0.2 M KCL and connected to a Model 600 Series Electrochemical Analyzer/Workstation from CH Instruments, Inc. The CVs were run at a scan rate of 20 mV/s that was cycled between 0.0 and 1.0 V versus the reference.

Transmission Electron Microscopy (TEM). TEM was performed using a JEOL 2200FS transmission electron microscope equipped with a field emission electron source. TEM images were recorded from a specimen consisting of Pt-catalyst deposited onto an electron-transparent carbon film, with the film supported by a 200 mesh copper grid.

Scanning Electron Microscopy (SEM). All SEM micrographs were obtained from a Carl Zeiss SMT Supra 55, a Schottky thermal field emitting microscope, with a five-axis stage. A primary beam voltage setting of 20 kV and a stage tilt of 10° were used during SEM imaging. No special sample processing was taken before imaging.

■ ASSOCIATED CONTENT

ⓢ Supporting Information

Experimental and characterization data including SEM imaging, XPS elemental analysis, N_2 absorption isotherms, ferricyanide cyclic voltammograms, and supporting videos. This material is available free of charge via the Internet at http://pubs.acs.org.

■ AUTHOR INFORMATION

Corresponding Author
*E-mail: jcclauss@iastate.edu.

Notes
The authors declare no competing financial interest.

■ REFERENCES

(1) Nawroth, J. C.; Lee, H.; Feinberg, A. W.; Ripplinger, C. M.; McCain, M. L.; Grosberg, A.; Dabiri, J. O.; Parker, K. K. A Tissue-engineered Jellyfish with Biomimetic Propulsion. *Nat. Biotechnol.* **2012**, *30*, 792−797.

(2) Pennisi, E. Manta Machines. *Science* **2011**, *332*, 1028−1029.

(3) Triantafyllou, M. S.; Triantafyllou, G. S. An Efficient Swimming Machine. *Sci. Am.* **1995**, *272*, 64−71.

(4) Mohseni, K. Pulsatile Vortex Generators for Low-Speed Maneuvering of Small Underwater Vehicles. *Ocean Eng.* **2006**, *33*, 2209−2223.

(5) Wernimont, E. J. *In Monopropellant Hydrogen Peroxide Rocket Systems: Optimum for Small Scale*, 42nd AIAA/ASME/SAE/ASEE Joint Propulsion Conference & Exhibit, Sacramento, Aerospace Research Central: Sacremento, 2006.

(6) Gordon, S.; McBride, B. J. In *Computer Program for Calculation of Complex Chemical Equilibrium Compositions and Applications*, Technical Report NASA Report, SP-273; Cleveland, OH, 1994; p 1311.

(7) De Groot, W. In *Propulsion Options For Primary Thrust And Attitude Control Of Microspacecraft*, Proceedings of COSPAR Colloquiium on Microsatellites, Taiwan, Pergamon Press: Taiwan, 1997; pp 200−209.

(8) Wang, J.; Gao, W. Nano/Microscale Motors: Biomedical Opportunities and Challenges. *ACS Nano* **2012**, *6*, 5745−5751.

(9) Mallouk, T. E.; Sen, A. Powering Nanorobots. *Sci. Am.* **2009**, *300*, 72−77.

(10) Wilson, D. A.; Nolte, R. J.; van Hest, J. C. Autonomous Movement of Platinum-Loaded Stomatocytes. *Nat. Chem.* **2012**, *4*, 268−274.

(11) Sanchez, S.; Solovev, A. A.; Mei, Y.; Schmidt, O. G. Dynamics of Biocatalytic Microengines Mediated by Variable Friction Control. *J. Am. Chem. Soc.* **2010**, *132*, 13144−13145.

(12) Campuzano, S.; Orozco, J.; Kagan, D.; Guix, M.; Gao, W.; Sattayasamitsathit, S.; Claussen, J. C.; Merkoçi, A.; Wang, J. Bacterial Isolation by Lectin-Modified Microengines. *Nano Lett.* **2011**, *12*, 396−401.

(13) Manesh, K. M.; Cardona, M.; Yuan, R.; Clark, M.; Kagan, D.; Balasubramanian, S.; Wang, J. Template-Assisted Fabrication of Salt-Independent Catalytic Tubular Microengines. *ACS Nano* **2010**, *4*, 1799−1804.

(14) Mirkovic, T.; Zacharia, N. S.; Scholes, G. D.; Ozin, G. A. Fuel for Thought: Chemically Powered Nanomotors Out-Swim Nature's Flagellated Bacteria. *ACS Nano* **2010**, *4*, 1782−1789.

(15) Orozco, J.; Jurado-Sánchez, B.; Wagner, G.; Gao, W.; Vazquez-Duhalt, R.; Sattayasamitsathit, S.; Galarnyk, M.; Cortés, A.; Saintillan, D.; Wang, J. Bubble-Propelled Micromotors for Enhanced Transport of Passive Tracers. *Langmuir* **2014**, *30* (18), 5082−5087.

(16) Soler, L.; Magdanz, V.; Fomin, V. M.; Sanchez, S.; Schmidt, O. G. Self-Propelled Micromotors for Cleaning Polluted Water. *ACS Nano* **2013**, *7* (11), 9611−9620.

(17) Solovev, A. A.; Mei, Y.; Bermúdez Ureña, E.; Huang, G.; Schmidt, O. G. Catalytic Microtubular Jet Engines Self-Propelled by Accumulated Gas Bubbles. *Small* **2009**, *5* (14), 1688−1692.

(18) Wang, H.; Moo, J. G. S.; Pumera, M. Tissue Cell Assisted Fabrication of Tubular Catalytic Platinum Microengines. *Nanoscale* **2014**, DOI: 10.1039/C4NR03720K.

(19) Wang, Y.; Hernandez, R. M.; Bartlett, D. J.; Bingham, J. M.; Kline, T. R.; Sen, A.; Mallouk, T. E. Bipolar Electrochemical Mechanism for the Propulsion of Catalytic Nanomotors in Hydrogen Peroxide Solutions. *Langmuir* **2006**, *22*, 10451−10456.

(20) Morgan, A. R.; Dawson, A. B.; McKenzie, H. S.; Skelhon, T. S.; Beanland, R.; Franks, H. P. W.; Bon, S. A. F. Chemotaxis Of Catalytic Silica-Manganese Oxide ″Matchstick″ Particles. *Mater. Horiz.* **2014**, *1*, 65−68.

(21) Laocharoensuk, R.; Burdick, J.; Wang, J. Carbon-Nanotube-Induced Acceleration of Catalytic Nanomotors. *ACS Nano* **2008**, *2* (5), 1069−1075.

(22) Paxton, W. F.; Kistler, K. C.; Olmeda, C. C.; Sen, A.; St. Angelo, S. K.; Cao, Y.; Mallouk, T. E.; Lammert, P. E.; Crespi, V. H. Catalytic Nanomotors: Autonomous Movement of Striped Nanorods. *J. Am. Chem. Soc.* **2004**, *126* (41), 13424−13431.

(23) Sattayasamitsathit, S.; Gao, W.; Calvo-Marzal, P.; Manesh, K. M.; Wang, J. Simplified Cost-Effective Preparation of High-Performance Ag−Pt Nanowire Motors. *ChemPhysChem* **2010**, *11* (13), 2802−2805.

(24) Baraban, L.; Makarov, D.; Streubel, R.; Monch, I.; Grimm, D.; Sanchez, S.; Schmidt, O. G. Catalytic Janus Motors on Microfluidic Chip: Deterministic Motion for Targeted Cargo Delivery. *ACS Nano* **2012**, *4*, 3383−3389.

(25) Gibbs, J. G.; Zhao, Y. P. Autonomously Motile Catalytic Nanomotors by Bubble Propulsion. *Appl. Phys. Lett.* **2009**, *94*, 163104.

(26) Ebbens, S. J.; Howse, J. R. Direct Observation of the Direction of Motion for Spherical Catalytic Swimmers. *Langmuir* **2011**, *27* (20), 12293−12296.

(27) Gao, W.; Pei, A.; Feng, X.; Hennessy, C.; Wang, J. Organized Self-Assembly of Janus Micromotors with Hydrophobic Hemispheres. *J. Am. Chem. Soc.* **2013**, *135* (3), 998−1001.

(28) Howse, J. R.; Jones, R. A. L.; Ryan, A. J.; Gough, T.; Vafabakhsh, R.; Golestanian, R. Self-Motile Colloidal Particles: From Directed Propulsion to Random Walk. *Phys. Rev. Lett.* **2007**, *99* (4), 048102.

(29) An, S.; Lim, H.; Kwon, S. In *Hydrogen Peroxide Thruster Module For Microsatellites With Platinum Supported By Alumina As Catalyst*, 43rd Joint Propulsion Conference and Exhibit, Cincinnati, Aerospace Research Central: Cincinnati, 2007; pp 8−11.

(30) Takahashi, K.; Ikuta, T.; Dan, Y.; Nagayama, K.; Kishida, M. In *Catalytic Porous Microchannel for Hydrogen Peroxide MEMS Thruster*, Proceedings of the 23rd Sensor Symposium, 2006; pp 513−516.

(31) Nicole, L.; Rozes, L.; Sanchez, C. Integrative Approaches to Hybrid Multifunctional Materials: From Multidisciplinary Research to Applied Technologies. *Adv. Mater.* **2010**, *22*, 3208−3214.

(32) Sanchez, C.; Belleville, P.; Popall, M.; Nicole, L. Applications of Advanced Hybrid Organic−Inorganic Nanomaterials: From Laboratory to Market. *Chem. Soc. Rev.* **2011**, *40*, 696−753.

(33) Astruc, D.; Lu, F.; Aranzaes, J. R. Nanoparticles as Recyclable Catalysts: The Frontier Between Homogeneous and Heterogeneous Catalysis. *Angew. Chem., Int. Ed.* **2005**, *44*, 7852−7872.

(34) Moshfegh, A. Nanoparticle Catalysts. *J. Phys. D: Appl. Phys.* **2009**, *42*, 233001.

(35) Jawale, D. V.; Gravel, E.; Geertsen, V.; Li, H.; Sha, N.; Namboothiri, I. N. N.; Doris, E. Aerobic Oxidation of Phenols and Related Compounds Using Carbon Nanotube−Gold Nanohybrid Catalysts. *ChemCatChem* **2014**, *6*, 719−723.

(36) Zapata, P. A.; Faria, J.; Ruiz, M. P.; Resasco, D. E. Condensation/Hydrogenation of Biomass-Derived Oxygenates in Water/Oil Emulsions Stabilized by Nanohybrid Catalysts. *Top. Catal.* **2012**, *55*, 38−52.

(37) Liu, R. J.; Yu, X. L.; Zhang, G. J.; Zhang, S. J.; Cao, H. B.; Dolbecq, A.; Mialane, P.; Keita, B.; Zhi, L. J. Polyoxometalate-Mediated Green Synthesis of a 2D Silver Nanonet/Graphene Nanohybrid as a Synergistic Catalyst for the Oxygen Reduction Reaction. *J. Mater. Chem. A* **2013**, *1*, 11961−11969.

(38) San, B. H.; Kim, S.; Moh, S. H.; Lee, H.; Jung, D. Y.; Kim, K. K. Platinum Nanoparticles Encapsulated by Aminopeptidase: A Multifunctional Bioinorganic Nanohybrid Catalyst. *Angew. Chem., Int. Ed.* **2011**, *50*, 11924−11929.

(39) Abbo, H. S.; Green, I. R.; Titinchi, S. J. J. In *Synthesis of Highly Dispersed Carbon Supported Platinum Nanocatalyst for Fuel Cells*, Proceedings of the ASME 9th International Conference on Fuel Cell Science, Engineering, and Technology, Washington, DC, Washington, DC, 2011; pp 891−892.

(40) Leong, G. J.; Schulze, M. C.; Strand, M. B.; Maloney, D.; Frisco, S. L.; Dinh, H. N.; Pivovar, B.; Richards, R. M. Shape-Directed Platinum Nanoparticle Synthesis: Nanoscale Design Of Novel Catalysts. *Appl. Organomet. Chem.* **2014**, *28*, 1−17.

(41) Zhang, G.; Sun, S.; Cai, M.; Zhang, Y.; Li, R.; Sun, X. Porous Dendritic Platinum Nanotubes With Extremely High Activity And Stability For Oxygen Reduction Reaction. *Sci. Rep.* **2013**, *3*, 1526.

(42) Wang, H.; Wang, Y.; Zhu, Z.; Sapi, A.; An, K.; Kennedy, G.; Michalak, W. D.; Somorjai, G. A. Influence Of Size-Induced Oxidation State Of Platinum Nanoparticles On Selectivity And Activity In Catalytic Methanol Oxidation In The Gas Phase. *Nano Lett.* **2013**, *13*, 2976−9.

(43) Burk, J. J.; Buratto, S. K. Electrodeposition of Pt Nanoparticle Catalysts from $H_2Pt(OH)_6$ and Their Application in PEM Fuel Cells. *J. Phys. Chem. C* **2013**, *117*, 18957−18966.

(44) Claussen, J. C.; Artiles, M. S.; McLamore, E. S.; Mohanty, S.; Shi, J.; Rickus, J. L.; Fisher, T. S.; Porterfield, D. M. Electrochemical Glutamate Biosensing with Nanocube and Nanosphere Augmented Single-Walled Carbon Nanotube Networks: A Comparative Study. *J. Mater. Chem.* **2011**, *21*, 11224−11231.

(45) Claussen, J. C.; Hengenius, J. B.; Wickner, M. M.; Fisher, T. S.; Umulis, D. M.; Porterfield, D. M. Effects of Carbon Nanotube-Tethered Nanosphere Density on Amperometric Biosensing: Simulation and Experiment. *J. Phys. Chem. C* **2011**, *115*, 20896−20904.

(46) Hrapovic, S.; Liu, Y.; Male, K. B.; Luong, J. H. Electrochemical Biosensing Platforms Using Platinum Nanoparticles and Carbon Nanotubes. *Anal. Chem.* **2004**, *76*, 1083−1088.

(47) Claussen, J. C.; Kumar, A.; Jaroch, D. B.; Khawaja, M. H.; Hibbard, A. B.; Porterfield, D. M.; Fisher, T. S. Nanostructuring Platinum Nanoparticles on Multilayered Graphene Petal Nanosheets for Electrochemical Biosensing. *Adv. Funct. Mater.* **2012**, *22*, 3399−3405.

(48) Yen, M.-Y.; Teng, C.-C.; Hsiao, M.-C.; Liu, P.-I.; Chuang, W.-P.; Ma, C.-C. M.; Hsieh, C.-K.; Tsai, M.-C.; Tsai, C.-H. Platinum Nanoparticles/Graphene Composite Catalyst as a Novel Composite Counter Electrode for High Performance Dye-Sensitized Solar Cells. *J. Mater. Chem.* **2011**, *21*, 12880−12888.

(49) Rioux, R.; Song, H.; Hoefelmeyer, J.; Yang, P.; Somorjai, G. High-Surface-Area Catalyst Design: Synthesis, Characterization, and Reaction Studies of Platinum Nanoparticles in Mesoporous SBA-15 Silica. *J. Phys. Chem. B* **2005**, *109*, 2192−2202.

(50) Kónya, Z.; Puntes, V. F.; Kiricsi, I.; Zhu, J.; Alivisatos, P.; Somorjai, G. A. Novel Two-Step Synthesis of Controlled Size and Shape Platinum Nanoparticles Encapsulated in Mesoporous Silica. *Catal. Lett.* **2002**, *81*, 137−140.

(51) Bell, A. T. The Impact of Nanoscience on Heterogeneous Catalysis. *Science* **2003**, *299*, 1688−1691.

(52) Chowdhury, A. D.; Bhaduri, S.; Lahiri, G. K. Is a Naked Platinum Nanocatalyst Better than the Analogous Supported Catalysts? *RSC Adv.* **2013**, *3*, 5341−5344.

(53) Meng, H.; Xie, F.; Chen, J.; Sun, S.; Shen, P. K. Morphology Controllable Growth of Pt Nanoparticles/Nanowires on Carbon Powders and its Application as Novel Electro-Catalyst For Methanol Oxidation. *Nanoscale* **2011**, *3*, 5041−8.

(54) Sun, S.; Jaouen, F.; Dodelet, J.-P. Controlled Growth of Pt Nanowires on Carbon Nanospheres and Their Enhanced Performance as Electrocatalysts in PEM Fuel Cells. *Adv. Mater.* **2008**, *20*, 3900−3904.

(55) Sun, S.; Zhang, G.; Geng, D.; Chen, Y.; Banis, M. N.; Li, R.; Cai, M.; Sun, X. Direct Growth of Single-Crystal Pt Nanowires on Sn@ CNT Nanocable: 3D Electrodes for Highly Active Electrocatalysts. *Chem.—Eur. J.* **2010**, *16*, 829−35.

(56) Sattayasamitsathit, S.; Gu, Y.; Kaufmann, K.; Jia, W.; Xiao, X.; Rodriguez, M.; Minteer, S.; Cha, J.; Burckel, D. B.; Wang, C.; Polsky,

R.; Wang, J. Highly Ordered Multilayered 3D Graphene Decorated with Metal Nanoparticles. *J. Mater. Chem. A* **2013**, *1*, 1639−1645.

(57) Fu, X.; Wang, Y.; Wu, N.; Gui, L.; Tang, Y. Preparation of Colloidal Solutions of Thin Platinum Nanowires. *J. Mater. Chem.* **2003**, *13*, 1192−1195.

(58) Henglein, A.; Ershov, B. G.; Malow, M. Absorption Spectrum and Some Chemical Reactions of Colloidal Platinum in Aqueous Solution. *J. Phys. Chem.* **1995**, *99*, 14129−14136.

(59) Chen, J.; Herricks, T.; Geissler, M.; Xia, Y. Single-Crystal Nanowires of Platinum Can Be Synthesized by Controlling the Reaction Rate of a Polyol Process. *J. Am. Chem. Soc.* **2004**, *126*, 10854−10855.

(60) Hoefelmeyer, J. D.; Niesz, K.; Somorjai, G. A.; Tilley, T. D. Radial Anisotropic Growth of Rhodium Nanoparticles. *Nano Lett.* **2005**, *5*, 435−438.

(61) Ahmadi, T. S.; Wang, Z. L.; Green, T. C.; Henglein, A.; El-Sayed, M. A. Shape-Controlled Synthesis of Colloidal Platinum Nanoparticles. *Science* **1996**, *272*, 1924−1925.

(62) Jung, M.-C.; Kim, H.-D.; Han, M.; Jo, W.; Kim, D. C. X-Ray Photoelectron Spectroscopy Study of Pt-Oxide Thin Films Deposited by Reactive Sputtering Using O_2/Ar Gas Mixtures. *Jpn. J. Appl. Phys.* **1999**, *38*, 4872−4875.

(63) Parkinson, C.; Walker, M.; McConville, C. Reaction of Atomic Oxygen with A Pt (111) Surface: Chemical and Structural Determination Using XPS, CAICISS And LEED. *Surf. Sci.* **2003**, *545*, 19−33.

(64) McKee, D. W. Catalytic Decomposition of Hydrogen Peroxide by Metals and Alloys of the Platinum Group. *J. Catal.* **1969**, *14*, 355−364.

(65) Friedman, H. L. Kinetics of Thermal Degradation of Char-Forming Plastics From Thermogravimetry. Application to a Phenolic Plastic. *J. Polym. Sci., Part C: Polym. Symp.* **1964**, *6*, 183−195.

(66) Lv, X.; Weng, J. Ternary Composite of Hemin, Gold Nanoparticles and Graphene for Highly Efficient Decomposition of Hydrogen Peroxide. *Sci. Rep.* **2013**, *3*, 3285.

(67) Wang, Z.; Lv, X.; Weng, J. High Peroxidase Catalytic Activity of Exfoliated Few-Layer Graphene. *Carbon* **2013**, *62*, 51−60.

(68) Hasnat, M. A.; Rahman, M. M.; Borhanuddin, S. M.; Siddiqua, A.; Bahadur, N. M.; Karim, M. R. Efficient Hydrogen Peroxide Decomposition on Bimetallic Pt−Pd Surfaces. *Catal. Commun.* **2010**, *12*, 286−291.

(69) Ma, Y.; Meng, S.; Qin, M.; Liu, H.; Wei, Y. New Insight on Kinetics of Catalytic Decomposition of Hydrogen Peroxide on Ferrihydrite: Based on the Preparation Procedures of Ferrihydrite. *J. Phys. Chem. Solids* **2012**, *73*, 30−34.

(70) Huang, C. P.; Huang, Y. F.; Cheng, H. P.; Huang, Y. H. Kinetic Study of an Immobilized Iron Oxide for Catalytic Degradation of Azo Dye Reactive Black B with Catalytic Decomposition of Hydrogen Peroxide. *Catal. Commun.* **2009**, *10*, 561−566.

(71) Chirita, P. A Kinetic Study of Hydrogen Peroxide Decomposition in Presence of Pyrite. *Chem. Biochem. Eng. Q.* **2007**, *21*, 257−264.

(72) Ramamurti, R.; Sandberg, W. C. In *Computational Fluid Dynamics Study for Optimization of a Fin Design*, 24th AIAA Applied Aerodynamics Conference, San Francisco, Aerospace Research Central: San Francisco, 2006; p 5235.

(73) Abershitz, A.; Penn, D.; Levy, A.; Shapira, A.; Shavit, Z.; Tsach, S. In *IAI's Micro/Mini UAV Systems-Development Approach*, Infotech@ Aerospace AIAA, Arlington, Aerospace Research Central: Arlington, 2005; pp 26−29.

(74) Watson, S. A.; Green, P. N. In *Propulsion systems for micro-autonomous underwater vehicles (μAUVs)*, IEEE Robotics Automation and Mechatronics (RAM) Singapore, IEEE: Singapore, 2010; pp 435−440.